MSL
ACADEMIC ENDEAVORS

Cleveland State University
EngagedScholarship@CSU

Chemical & Biomedical Engineering Faculty Publications

Chemical & Biomedical Engineering Department

11-15-2018

Effect of Cross-Section-Change Induced Advective Flow on the Primary Dendrite Array Morphology of Hypoeutectic Pb-Sb Alloys During Directional Solidification

K. Pandit
Cleveland State University

S. R. Upadhyay
Cleveland State University

Surendra N. Tewari
Cleveland State University

Follow this and additional works at: https://engagedscholarship.csuohio.edu/encbe_facpub

Part of the Chemical Engineering Commons, and the Materials Science and Engineering Commons
How does access to this work benefit you? Let us know!

Publisher's Statement
https://doi.org/10.1016/j.jcrysgro.2018.09.005

Repository Citation

Effect of cross-section-change induced advective flow on the primary dendrite array morphology of hypoeutectic Pb-Sb alloys during directional solidification

K. Pandit, S.R. Upadhyay, S.N. Tewari

ABSTRACT

The morphology and distribution of primary dendrites have been examined in Pb-2.2, 5.8 and 10.8 wt. pct. Sb alloy samples directionally solidified (DSed) in ampoules shaped like an hour-glass to examine the influence of cross-section change induced advective flow on the cellular/dendritic interface. This sample design increases the advective flow of the melt towards the array tips, as the liquid-solid interface enters the neck of the ampoule, and then decreases it as the interface exits the neck. The warm solute-rich melt flowing towards the growth front suppresses the extent of side-branching, decreases the primary dendrite spacing, and increases the primary dendrite trunk diameter as observed in the Pb-5.8 and 10.8 Sb alloys. The flow appears to suppress the formation of cells. A cellular interface growing in the Pb-2.2Sb alloy became planar as the solidification front entered the neck, becoming cellular again as it exited the neck.

1. Introduction

Ideally the primary dendrite arms in superalloy single crystal castings are uniformly distributed and all are in a ⟨1 0 0⟩ orientation parallel to the blade axis, without sub-grains. The molds for these castings contain ceramic cores. Solidification thus progresses through several cross-sectional changes. In addition, the helical grain selector at the bottom and the platforms at the root and the tip of the blade introduce other major section changes. Castings with grain misalignment, low angle grain boundaries, spurious grains, "slivers" and "freckles" are rejected; all these defects are believed to be related to the convection at the cross-sectional changes. Effect of convection due to cross-sectional changes during directional solidification on the radial and axial macrosegregation [1–15], and on the formation of stray grains [16–23] have been extensively investigated. The effect of cross-section-change induced advective flow on the dendrite-array morphology, however, has not been studied.

The influence of forced convection on the dendrite array morphology has been examined by superimposing a shear-flow (transverse to the growth direction) during solidification of transparent organic model "alloys" [24–30] and of Ga-25In [31,32]. The influence of natural convection on the dendrite array morphology has been studied by, (i) comparing morphologies observed in samples solidified in larger diameter ampoules with those grown in smaller diameter ampoules or within narrow-gaps in order to mitigate convection [33,34], (ii) selecting alloy compositions and growth conditions which promote buoyancy flows in the mushy zone either towards the tips of the primary dendrites or towards their base [35,36], (iii) comparing microstructures of alloys solidified on earth with those grown in the low-gravity environment of space [35–44], (iv) using magnetic fields during directional solidification to suppress [45] or enhance convection [46–48], and (v) by developing semi-empirical formulations [45] that qualitatively explain the discrepancy between the observed primary spacings and those predicted from models which are based on purely diffusive transport. Numerical simulation attempts, both two and three dimensional, have been made to study the relationship between convection and dendrite morphology [48–52]. However, because of the computational limitations, a numerical analysis which truly incorporates the three-dimensional complex inter-dependence of the dendrite morphology, the mushy-zone permeability, and the imposed convection has not been possible.

Theoretical models have shown that "shear flow" suppresses the onset of morphological instability [24–26]. Directional solidification experiments with imposed shear flows have been carried out on succinonitrile-acetone [27,28], succinonitrile-camphor [29], or cyclohexanol [30], in gaps (200–300 μm) between glass slides. These

experiments showed that cells bend towards the downstream of shear flow [27] and that dendrites bend towards the upstream [27–30]. Side-branching was enhanced upstream of the primary dendrite arms and suppressed downstream [27–30]. Also, the primary dendrite spacing was significantly larger in the presence of shear-flow than that without any imposed convection [29,30]. Imposed shear flow has been shown to promote growth of side-branches at the upstream side of primary dendrites in Ga-25In alloy [31].

Effect of sudden change in cross section was studied by Fabietti et al. [53] on succinonitrile-acetone alloys in thin (~150 μm) transparent glass crucibles. For a constant translation speed, the interface velocity was observed to decrease as the interface entered the narrow cross-section, this resulted in an initially planar shape becoming cellular, and a cellular shape becoming dendritic. However, when the minimum cross-section was about five times the primary spacing, no appreciable change was observed when the dendrite array traveled across the cross-sectional change. In these experiments, however, the wall-effects might have distorted the array morphology, and the Lewis Number of these materials is three orders of magnitude smaller than that of the metals. Thus, the true three-dimensional behavior of dendrite arrays was missed.

Primary dendrite spacing in metallic alloy samples grown in the low-gravity, reduced convection, environment of space was observed to be larger than in the samples grown terrestrially in the presence of natural convection, 11% larger in Al-3.5 wt.%[2] Li [41], 30% larger in Cu-29Mn [42], 36% larger in Al-1.5Ni [41] and four and half times larger in Al-26Cu [35,37]. This was also true for the faceted $CuAl_2$ dendrites in the hyper-eutectic Al-40Cu [35]. Observation of larger spacing in microgravity processed samples in the absence of terrestrial natural convection is contrary to the primary spacing increase observed in the presence of convection imposed by shear flow [29,30].

Attempts were made to suppress convection during dendritic arrayed growth of metallic alloys by superimposing axial magnetic fields and by reducing the crucible diameter. The application of transverse magnetic field, however, did not suppress convection; instead it distorted the morphology of the mushy zone because of the anisotropy in the fluid flow [45,47]. It has been shown that capillary diameters significantly less than 1-mm are required to eliminate convection during directional solidification of Al-4Cu alloy [33]. The use of such a small ampoule diameter would allow growth of only one or two dendrites that are significantly constrained by the wall effects. It is impossible to grow a dendrite array with the usually observed 100–300 μm spacing in these capillaries.

The contradictory observations described above, larger primary dendrite spacing in the presence of convection due to shear-flow than that in its absence [29,30] and increased primary dendrite spacing in low gravity grown (reduced convection) samples as compared with those terrestrially solidified [35–42], suggest that the nature of convection may be quite different under the two circumstances; i.e., changes of the dendrite morphology resulting from convection due to shear flows do not represent those that are associated with the thermosolutal convection during terrestrial directional solidification. A true understanding of the effect of natural convection on the dendritic array morphology and its distribution cannot be attained by imposing only a transverse flow. Superimposing a flow that is either parallel or anti-parallel to the growth direction, however, is very difficult during directional solidification as compared to the transverse shear flow. Perhaps that is the reason why only the effects of imposed shear flows on the cellular-dendritic morphology and its ordering have been systematically studied so far, not the effect of parallel flow.

The purpose of this study was to examine the role of the cross-section change induced axial advective flow towards or away from the

liquid-solid interface on the cellular/dendrite array morphology and ordering during directional solidification of metallic alloys by using hour-glass shaped ampoules. It is seen that for a dendritic array the increased flow toward the growth front suppresses the extent of side-branching and decreases the primary dendrite spacing. For a cellular array it can suppress the side-branching completely and yield a planar liquid-solid interface. It also increases the trunk diameter of primary dendrites.

2. Experimental

2.1. Alloy preparation and directional solidification

Three alloys representing varying mushy zone permeability, Pb-2.2Sb, Pb-5.8Sb and Pb-10.8Sb were prepared by melting together lead and antimony (99.99% purity) in an argon environment. The mushy zone is more permeable for the 5.8Sb alloy than for the 2.2Sb; the freezing range and the fraction eutectic are 61 K and 9% for the 2.2Sb alloy, and 36 K and 42% for the 5.8Sb alloy. The 10.8Sb alloy is very close to the eutectic (Pb-11.2 wt. pct. Sb) and has very small fraction solid ~6%.
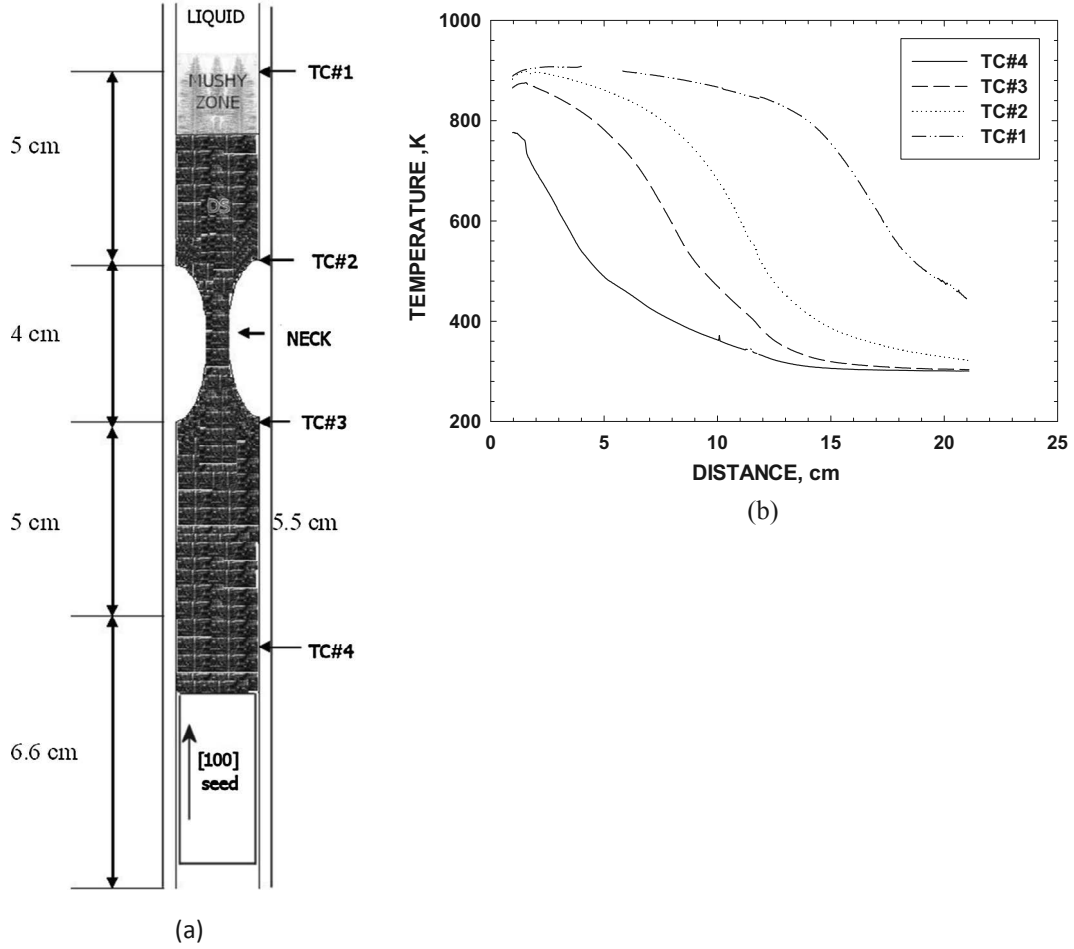
Directional solidification was carried out in ampoules shaped like an hour-glass, schematically shown in Fig. 1(a). This sample design increases the advective flow towards the interface as the liquid-solid interface enters the neck of the ampoule and decreases the flow as the interface exits the neck. The "hour-glass" ampoule made from 7-mm I.D. quartz tube was placed inside a larger diameter (12-mm I.D.) ampoule, also filled by the identical alloy charge, to mitigate radial gradients at the growth front. The ampoule neck was approximately 4-cm long. The minimum diameter at the neck ranged from 3 to 4-mm in various ampoules. A 2-cm long lead single crystal (⟨1 0 0⟩ parallel to the growth direction) seeded the solidification of either Pb-2.2Sb, Pb-5.8Sb or Pb-10.8 Sb alloy kept above the seed. Directional solidification was carried out by withdrawing the hot-zone of the furnace up-wards at two growth speeds: 2.5 μm s^{-1} and 30 μm s^{-1}, while the quartz ampoule remained stationary. Both experiments were carried out under a thermal gradient at the liquidus (G_l) of about 82 K cm^{-1}. Total length of about 14 to 16-cm of the sample was solidified.

In one of the experiments, four 0.5-mm chromel-alumel thermocouples, enclosed in 1-mm quartz capillaries, were also inserted in the inner "ampoule" and placed along its length in order to measure the thermal gradients in the melt ahead of the dendritic array as the array tip traversed along the ampoule length. The thermal profiles recorded by the four thermocouples (TC#1 through TC#4) during directional solidification of Pb-5.8Sb alloy at 30 μm s^{-1}, with the furnace hot zone temperature of 873 K is shown in Fig. 1(b). This figure shows that the thermal gradients in the solidifying sample were not affected by the variation in the ampoule cross-section area. The G_l values obtained from the TC#4, TC#3, TC#2, and TC#1 temperature profiles, are 82, 84, 87 and 72 K cm^{-1}, respectively. This indicates that a steady-state thermal profile in the mushy-zone was maintained during directional solidification process along the sample length, except near the top end of the samples where TC#1 is located. The unusually low G_l of 72 K cm^{-1} recorded by TC#1 arises because by the time this thermocouple was at the liquidus temperature there was only 1-cm of melt column left to solidify, the rest of the sample length below was already solid. Since the thermal conductivity of the solid phase is about two times that of the liquid [54], a constant G_l can only be maintained as long as an adequate length of the melt column, and that of the solidified portion exist.

2.2. Metallography and statistical analysis of cell/dendrite distribution

Transverse microstructures were observed along the length of the DSed samples, below the constriction, at the constriction itself and above the constriction, by standard polishing and optical metallography

---

[2] In this paper wt.% is dropped so Pb-5.8 wt% Sb is simply designated as Pb-5.8Sb, and so on.

Fig. 1. Schematic of the hour-glass shaped ampoule used for directional solidification of Pb-Sb alloys and a typical thermal profile recorded during DS. (a) Schematic of the double-wall hour-glass shaped ampoule showing the 2-cm long, [1 0 0] oriented, single crystal seed at the bottom. The seed was partially re-melted and fused with the melt-stock above before directional solidification. The gap between the outer and inner walls of the ampoule was also filled by the alloy. (b) Thermal profiles recorded by the four thermocouples (TC#1 through TC#4) during a typical directional solidification of Pb-5.8Sb alloy at $30\,\mu\mathrm{m\,s^{-1}}$, with the furnace hot zone temperature of 873 K.

techniques. Montages of the microstructures recorded at 50 times magnification were created in order to obtain high resolution image of the entire sample cross-sections. Center of mass of the individual cells/primary dendrites in the entire sample cross-section were identified and electronically recorded as a table of (x,y) coordinates. Following measurements were made from these images.

(1) The minimum spanning tree based '*nearest neighbor spacing*' (λ_{MST}): Minimum spanning tree (MST) is a connected curve without any closed loop that contains all of the cell/primary-dendrite centers on the transverse section and has the shortest total branch-length [55]. Average value of the length of tree-branches (m*) and its standard deviation (σ*), provide a statistical measure of the nearest-neighbor distribution of the cells/primary-dendrites. It was shown by Dussert et al. [55] that the two parameters, m* and σ*, can be normalized by dividing them by the square root of the average cell surface < S > , obtained from the corresponding Voronoi tessellations, to yield m and σ, where,

$$m = \frac{m*}{\sqrt{<S>}}\frac{N-1}{N} \tag{1}$$

$$\sigma = \frac{\sigma*}{\sqrt{<S>}}\frac{N-1}{N} \tag{2}$$

The m vs. σ plots can be used to compare the arrangements with different nearest neighbor spacing distributions, including random

noise superimposed on the hexagonal or square lattices [55].

Fraction eutectic constituents (f_e) in the Pb-5.8Sb alloy samples were measured on the transverse microstructures in a manner similar to that described in Ref. [56].

3. Results

3.1. Dendritic array in medium permeability Pb-5.8Sb alloy

3.1.1. Well-branched primary dendrites

Fig. 2 shows the morphology and distribution of primary dendrites in a Pb-5.8Sb alloy DSed at $30\,\mu\mathrm{m\,s^{-1}}$ and $82\,\mathrm{K\,cm^{-1}}$. Transverse views of the entire sample cross-section area at 3-cm above the neck, at the neck, and at 5-cm below the neck, are presented in Fig. 2(a)–(c) respectively. These figures also contain higher magnification views in their inset. The primary dendrites are more branched in the sections below and above the necked portion of the sample (Fig. 2(b) and (d)); extent of side branching is less at the neck (Fig. 2(b)). The area-decrease induced shrinkage flow towards the array tips causes re-melting of side-branches, thus making the primary dendrites appear blunt. This observation is also confirmed by the shape factor measurement of the dendrites, as shown below. Fig. 2 also shows that for this well-branched primary dendrite sample the underlying square arrangement of side-arms initiated by the single-crystal seed was retained throughout the sample length, as the liquid-solid interface traversed through the neck
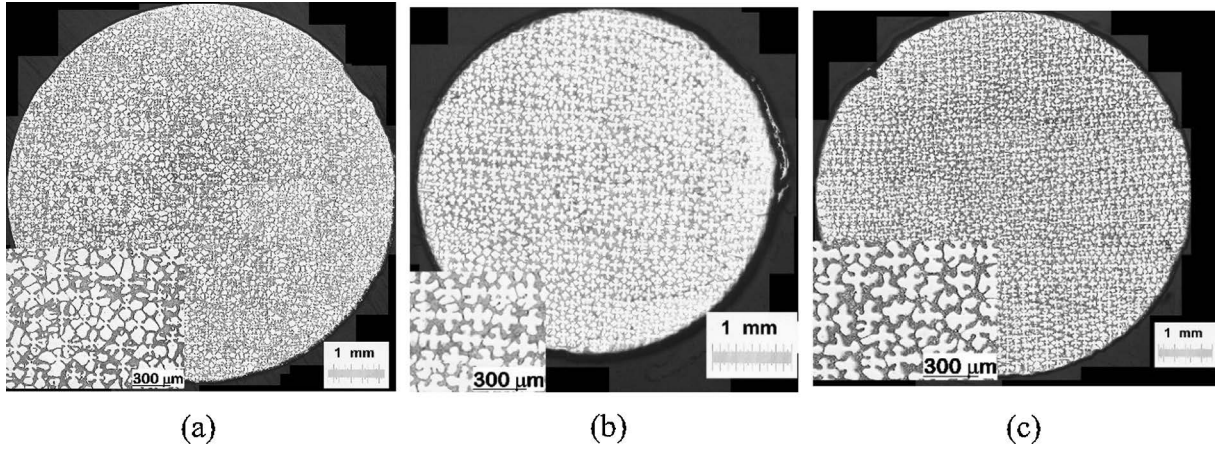
Fig. 2. The influence of cross-section-change driven flow on the primary dendrite morphology and distribution in a Pb-5.8 wt. pct. Sb alloy DSed at 30 $\mu m \, s^{-1}$ and 82 K cm^{-1}. (a) 3-cm above the neck, (b) at the neck, (c) 5-cm below the neck.

and came back up into the uniform cross-section portion of the ampoule, i.e., the cross-section change induced flow did not produce any additional stray grain.

Fig. 3 shows the variation in the spacing of primary dendrites, and

their shape factor. Fig. 3(a) shows the nearest-neighbor spacing distribution (determined from the MST branch-length distributions) as a function of distance from the neck. The 5, 10, 25, 50, 75, 90 and 95 percentile values from these distributions are indicated by their
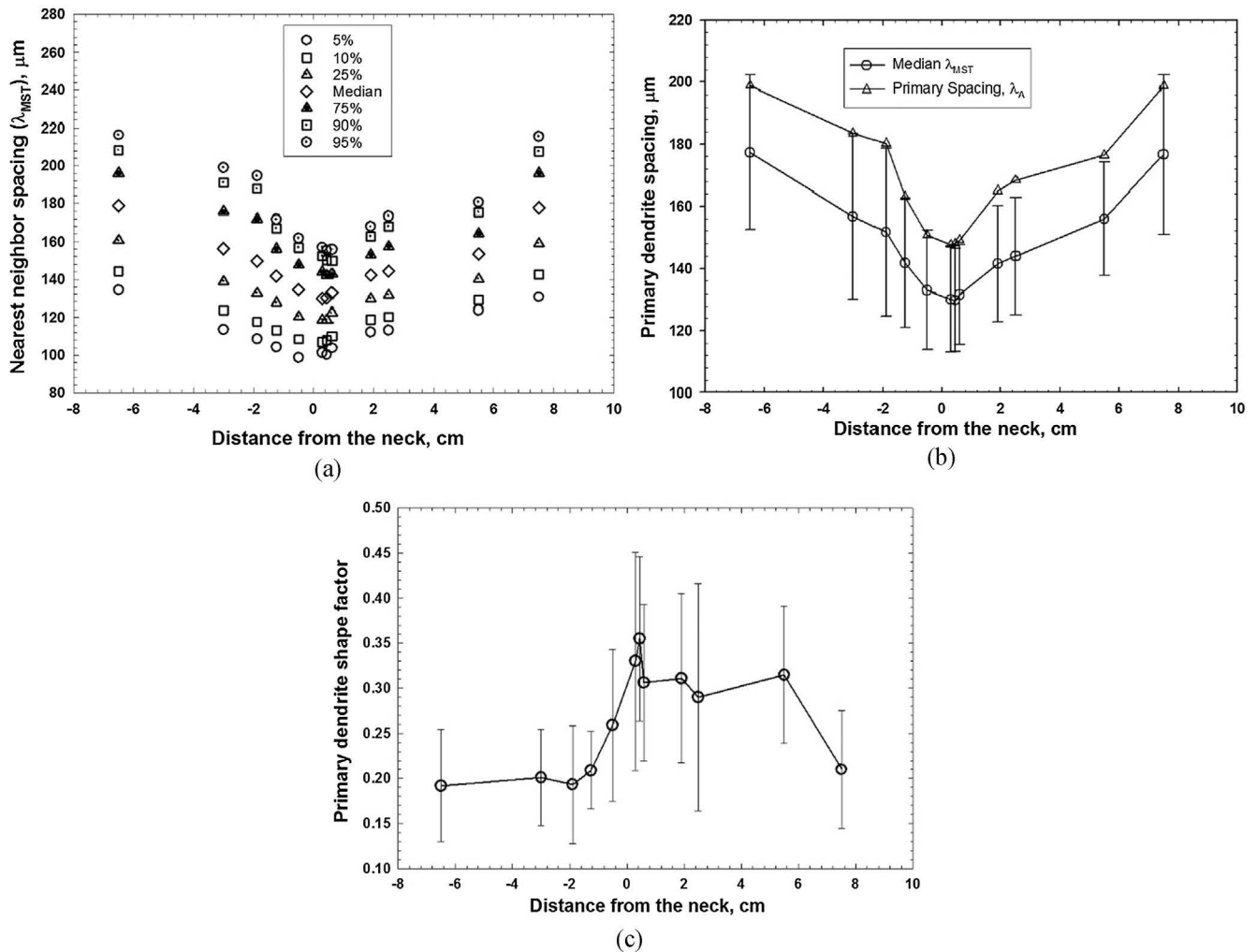

Fig. 3. Dendrite spacing and shape factor variation as a function of distance from the neck for the Pb-5.8 Sb alloy DSed at 30 $\mu m \, s^{-1}$ and 82 K cm^{-1}. (a) Nearest neighbor spacing (λ_{MST}) distribution (determined from the MST branch-length distributions). (b) Primary dendrite spacing variation along the sample length. The median nearest neighbor spacing (λ_{MST}) and its corresponding one standard deviation is indicated by circle symbols. The triangles correspond to the primary spacing, λ_A, obtained by the area method. (c) Dendrite shape factor variation.

respective symbols. There is a continued decrease in the nearest-neighbor spacing as the liquid-solid interface enters the neck, followed by an increase to its previous level as it exits the neck. It is interesting to note that the entire spacing distribution, the maximum, the median and the minimum, follows this trend.

Fig. 3(b) plots the median nearest-neighbor spacing (λ_{MST}) (indicated by circles) and its standard deviation, together with the primary spacing (λ_A) as determined by $\sqrt{A_0/(N-1)}$ (indicated by triangles). The λ_{MST} decreases from 180-μm to 125-μm as the liquid-solid interface approaches the neck; and it increases again back to 180-μm after the interface reaches above the neck. The same behavior is also indicated by the λ_A. It is interesting to note that the area-based primary arm spacing values are invariably higher than those determined by the MST method.

Decrease in the primary dendrite spacing is associated with melting of their side-branches as indicated by the dendrite shape-factor values shown in Fig. 3(c). This figure shows the variation in the dendrite shape-factor along the length of the sample, and its ± one standard deviation. The shape factor is about 0.2 in the bottom portion of the sample. It slowly rises as the liquid-solid interface moves into the neck reaching a maximum value of about 0.3 and begins to decrease as the interface moves away from the neck, ultimately reaching its original value of about 0.2. Let us recall that the shape factor is unity for circle and it decreases with an increase in the extent of side-branching. Fig. 3(c) confirms that the decrease in the primary dendrite spacing as the liquid-solid interface enters the neck portion of the hour-glass shaped ampoule is associated with the melting of side-branches.

3.1.2. Less-branched primary dendrites

Fig. 4 shows the effect of changing cross-section on the dendrite morphology and distribution in a Pb-5.8 Sb alloy sample that was DSed at 82 K cm^{-1} and 2.5 μm s^{-1}. This growth speed lies just above the cell to dendrite transition speed and produces stubbier and less branched primary dendrites than those grown at 30 μm s^{-1} (Fig. 2). Fig. 4(a) shows that the microstructure is initially dendritic as the liquid solid interface traverses the uniform cross-section portion of the quartz tube

below the neck. It changes from dendritic to cellular, as the liquid-solid interface approaches the constriction (Fig. 4(b) and (c)). As the interface traverses away from constriction, back into the uniform cross-section region above the neck, the morphology transforms back to dendritic (Fig. 4(d)–(f)).

Fig. 5(a) plots the corresponding nearest-neighbor spacing distributions determined from the MST-branch length distributions as a function of distance from the neck. For this sample, the primary dendrites having nearest-neighbor spacing larger than the median show the same behavior as described above for the well-branched primary dendrites (Fig. 3(a)); their spacing decreases as the interface enters the neck and increases again to its normal value as it exits the neck. The primary dendrites with nearest-neighbor spacing less than the median, however, remain unaffected by the cross-section change. Apparently on the same cross-section those primary arms which are more dendrite-like (with extensive side branches) and thus have the larger spacing are more affected by the cross-section change induced flow than those which are more cell-like and have smaller spacing. Fig. 5(b) plots the median nearest-neighbor spacing, λ_{MST}, (indicated by circles) and the primary spacing, λ_A, (indicated by triangles) as a function of distance from the neck. The area-based primary spacing decreases from an initial value of about 200-μm to about 175-μm at the neck. Then as the liquid-solid interface exits the neck, the value increases and becomes same as before the neck, about 200-μm. The decrease in this sample is, however, much smaller than 50-μm decrease observed for the Pb-5.8 Sb sample grown at 30 μm s^{-1} which had well-branched primary dendrites (Fig. 3(b)). The median nearest-neighbor spacing obtained from the MST branch length distribution also shows a similar behavior.

The corresponding shape factor change is shown in Fig. 5(c). As expected from the blunter dendrite morphology observed in this experiment, compared with the sample grown at 30 μm s^{-1}, the shape factor is higher; about 0.5 versus 0.2. There is a gradual increase in the shape factor from about 0.4 to about 0.7 as the liquid-solid interface moves towards the neck region of the hour-glass ampoule. This is followed by a decrease as the interface comes back into the constant cross-section region of the ampoule.
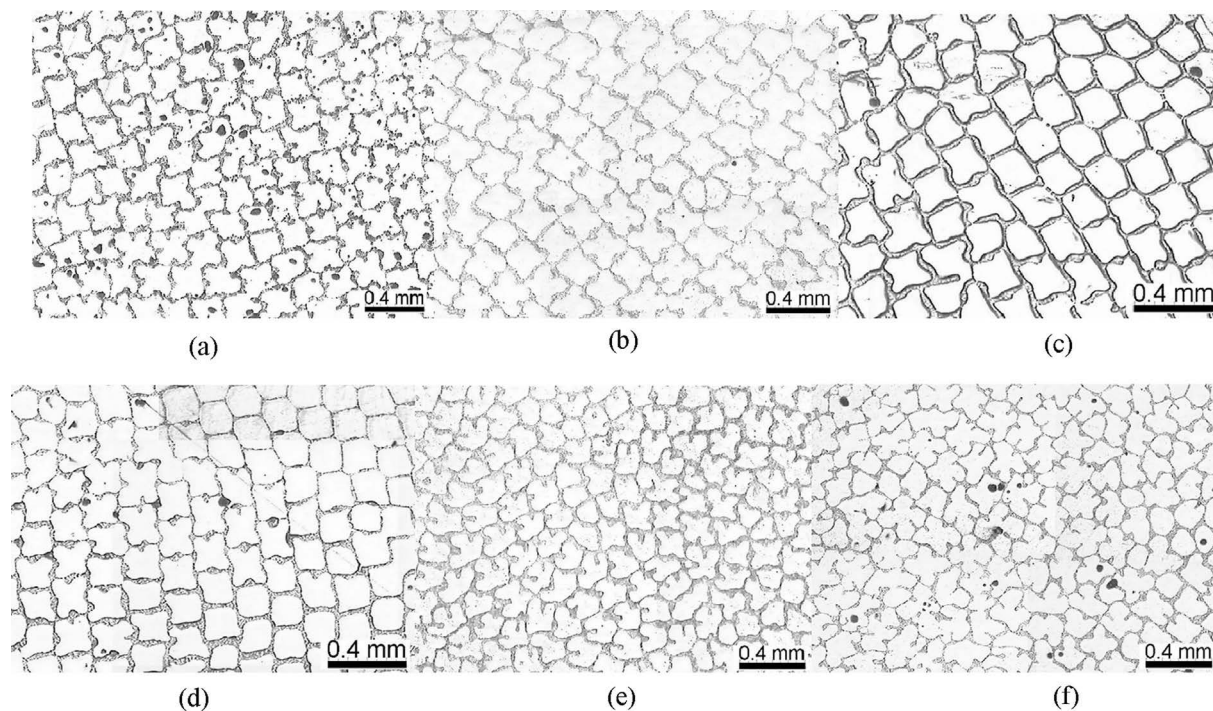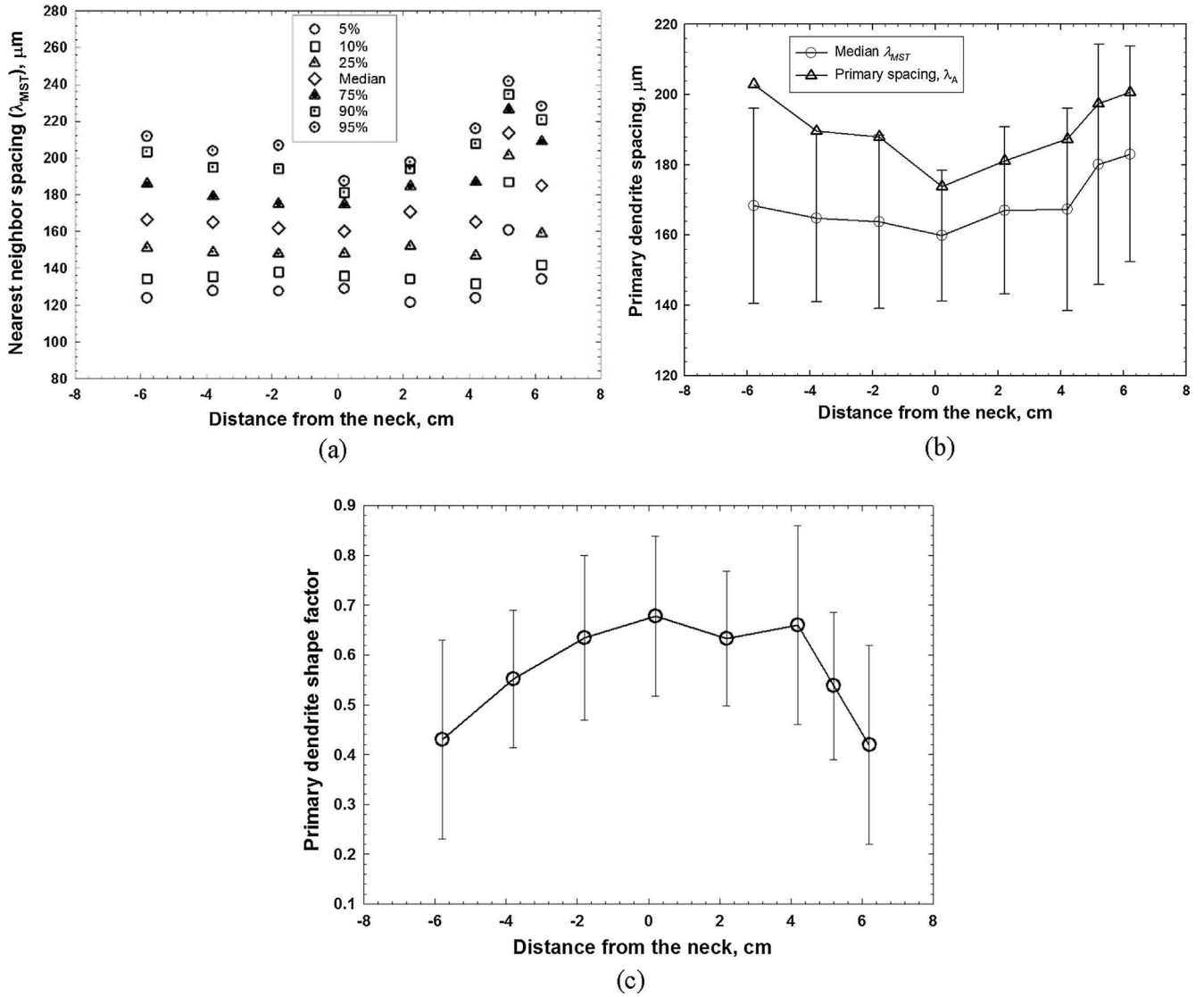

Fig. 4. Primary dendrite morphology and distribution on the transverse sections along the length of a Pb-5.8 Sb alloy DSed at 2.5 μm s^{-1} and 82 K cm^{-1} in an hour-glass shaped ampoule. (a) 5-cm below the neck, (b) 1-cm below the neck, (c) at the neck, (d) 6-mm above the neck, (e) 2-cm above the neck, and (f) 4-cm above the neck.

Fig. 5. Dendrite spacing and shape factor variation as a function of distance from the neck for the Pb-5.8Sb alloy DSed at 2.5 μm s^{-1} and 82 K cm^{-1}. (a) Nearest neighbor spacing (λ_{MST}) distribution (determined from the MST branch-length distributions). (b) Primary dendrite spacing variation along the sample length. The median nearest neighbor spacing (λ_{MST}) and its corresponding one standard deviation is indicated by circle symbols. The triangles correspond to the primary spacing, λ_A, obtained by the area method. (c) Dendrite shape factor variation.

3.2. Cellular array in low permeability Pb-2.2 Sb alloy

Fig. 6(a) shows the cellular array microstructure on transverse sections at 4-cm below the neck for Pb-2.2 Sb alloy solidified at 82 K cm^{-1} and 2.5 μm s^{-1}. The row-like appearance of the cells is an artifact due to joining of nearby cells. The liquid-solid interface becomes planar (feature-less) as it goes through the neck, Fig. 6(b). The cellular morphology again develops once the interface is in the constant cross-section portion of the ampoule as shown in Fig. 6(c), corresponding to 5-cm above the neck.

Fig. 7(a) shows that as the liquid-solid interface moves towards the neck, the nearest-neighbor spacing also begins to decrease; the entire nearest-neighbor spacing distribution (5, 10, 25, median, 75, 90 and 95 percentile) follows this trend. Since the morphology became planar at the neck there are no spacing data for that location. The spacing increases gradually again as the liquid-solid interface emerges from the neck and moves into the uniform cross-section portion of the ampoule. Both, the median nearest-neighbor spacing and the mean primary spacing, show similar behavior (Fig. 7(b)). The decrease in the primary spacing due to the cross-sectional area change for this sample is only

about 15-μm; this is much smaller than about 50-μm observed for the well-branched dendrite array described in Fig. 3(b). It was not possible to carry out a meaningful shape factor measurement due to the lack of clearly defined cell boundaries for the cell morphologies indicated in Fig. 6.

3.3. Dendritic array in high permeability Pb-10.8 Sb alloy

This hypoeutectic alloy composition is very close to the eutectic, Pb-11.2 Sb, and results in a small fraction of well-branched primary dendrites and a large volume fraction of interdendritic eutectic when it is DSed at 82 K cm^{-1} and 30 μm s^{-1} (Fig. 8). Insets show higher magnification views. The primary dendrites have long secondary side-branches with tertiary arms. The square grid of the primary dendrite distribution reflects the single crystal orientation brought about by the ⟨1 0 0⟩ seed. A comparison of Fig. 8(a) and (b) shows that as the liquid-solid interface approaches the neck, morphology of the primary dendrites changes drastically. There is a drastic decrease in the length of side-branches and the tertiary arms are absent; the primary dendrites are, therefore significantly blunter. Primary dendrites regain their
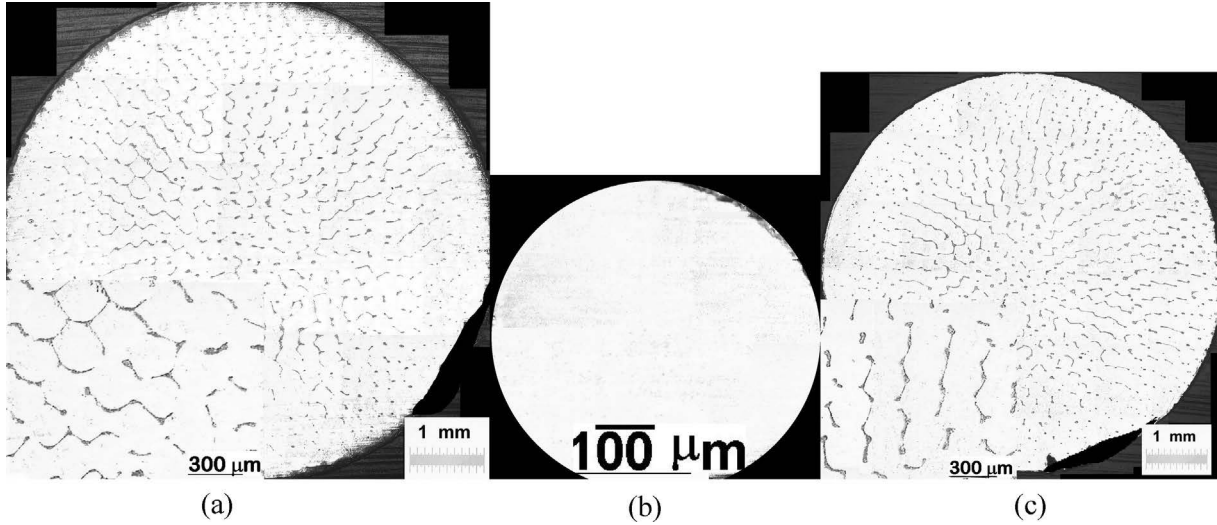
Fig. 6. Cellular array morphology and distribution on the transverse sections along the DSed length of Pb-2.2 Sb grown at 2.5 μm s⁻¹ and 82 K cm⁻¹ in an hour-glass shaped ampoule. (a) 4-cm below the neck, (b) at the neck, (c) 5-cm above the neck.

original morphology having long side-branches after the liquid-solid interface emerges from the neck, as shown in Fig. 8(c), 2-cm above the neck. They, however, no longer have the original four-fold square grid type of long range order seen in Fig. 8(a). This indicates extensive convection-driven sub-grain formation as the mushy zone passes through the constriction.

Fig. 9 shows the change in the nearest neighbor spacing distribution of primary dendrites along the length for this Pb-10.8 Sb sample grown at 82 K cm⁻¹ and 30 μm s⁻¹. The entire spacing distribution, from the largest to the smallest shows a decrease as the interface enters the neck. The spacing decrease due to the section change for this alloy is similar to that earlier described Pb-5.8 Sb alloy grown at 30 μm s⁻¹, about 60-μm.

3.4. Longitudinal macrosegregation in DSed Pb-5.8Sb samples

The hypoeutectic Pb-Sb alloys are susceptible to "plume-type" thermosolutal convection [11] during directional solidification, because the solute rich eutectic melt at the bottom of the mushy-zone

(11.8 wt. pct. Sb), is lighter than the solute poor melt at the array tips, about 5.8 wt. pct. Sb (ignoring the minimal solute build-up due to the dendrite tip curvature). The resulting convection continually sweeps the solute from the mushy-zone into the bulk melt ahead, as the sample is DSed. This makes the DSed portion of the sample solute poor, and the last liquid to freeze, solute rich [57–59]. The area fraction of the eutectic constituent (f_E) on a transverse microstructure is one measure of the local mean solute content. The Pb-5.8 Sb alloy is expected to have $f_E \sim 0.42$. Fig. 10(a) plots experimentally measured f_E on several cross-sections along the DSed length in the two 5.8 Sb samples grown at 2.5 and 30 μm s⁻¹. At 2.5 μm s⁻¹, f_E in the DSed portion is only 0.22 ± 0.04 (Fig. 10(a)), suggesting that at 2.5 μm s⁻¹ the 'plume type" thermosolutal convection was quite severe. The flow continually swept the solute from the solidifying mushy-zone into the melt column ahead, ultimately accumulating most of the solute in the last liquid left to freeze. At 30 μm s⁻¹, f_E is approximately 0.46 ± 0.03, which is close to 0.42, the value expected in the Pb-5.8 Sb alloy. It suggests that at 30 μm s⁻¹ the "plume type" thermosolutal convection was minimal. These observations are in agreement with the previously seen behavior;
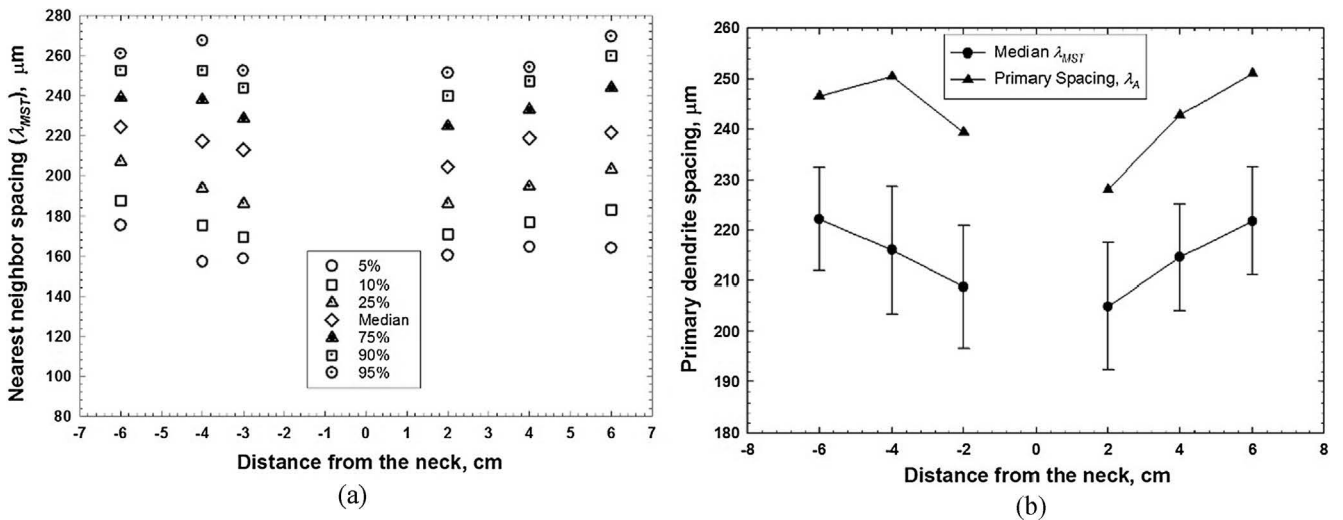

Fig. 7. Primary spacing variation of cells as a function of distance from the neck for the Pb-2.2Sb grown at 2.5 μm s⁻¹ and 82 K cm⁻¹. (a) Nearest neighbor spacing (λ_{MST}) distribution (determined from the MST branch-length distributions), (b) Primary dendrite spacing variation along the sample length. The median nearest neighbor spacing (λ_{MST}) and its corresponding one standard deviation is indicated by circle symbol. The triangles correspond to the primary spacing, λ_A, obtained from $\sqrt{A_0/(N-1)}$.
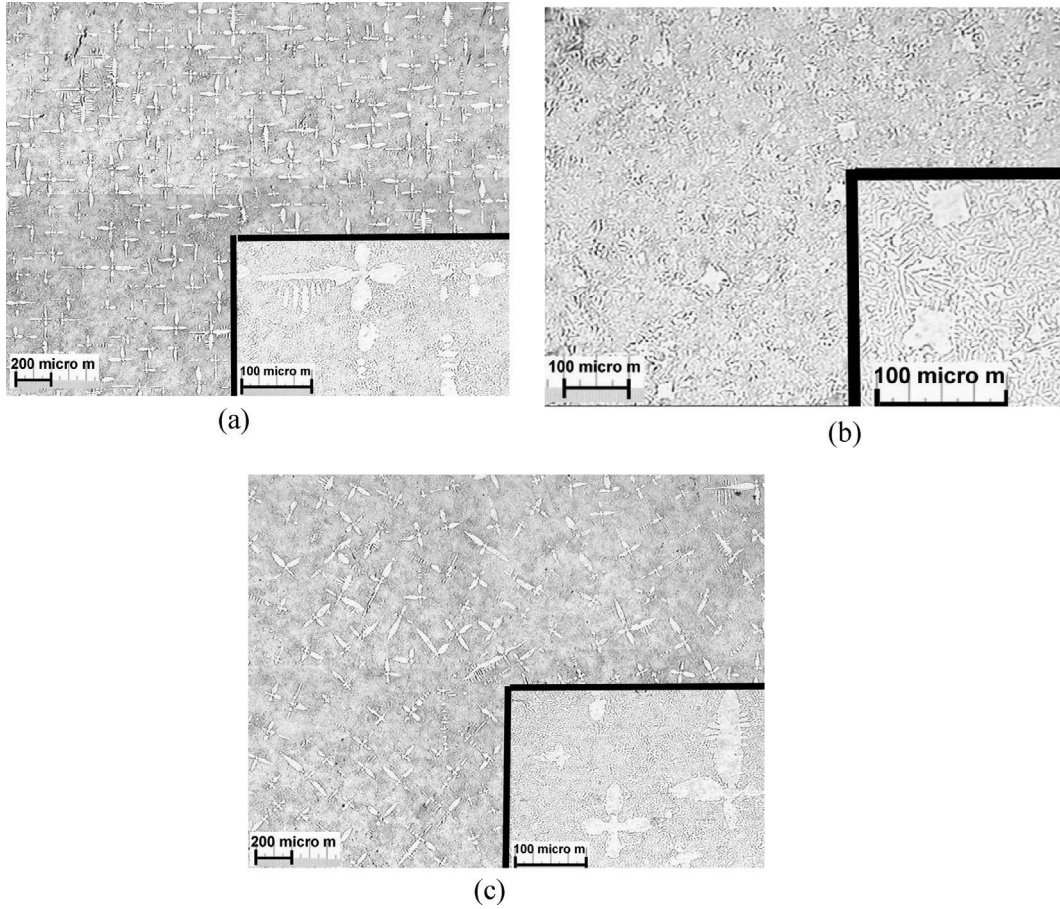
Fig. 8. Primary dendrite morphology and distribution on the transverse sections along the DSed length of Pb-10.8 Sb grown at $30\,\mu m\,s^{-1}$ and $82\,K\,cm^{-1}$ in an hourglass shaped ampoule. (a) 2-cm below the neck, (b) at the neck, (c) 2-cm above the neck. Insets present higher magnification views.
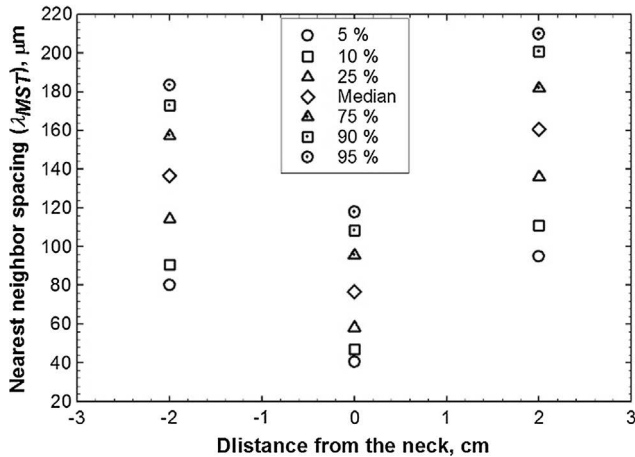

Fig. 9. Nearest neighbor spacing (λ_{MST}) distribution of primary dendrites (determined from the MST branch-length distributions) as a function of distance from the neck for the Pb-10.8 Sb alloy DSed at $30\,\mu m\,s^{-1}$ and $82\,K\,cm^{-1}$.

when the same alloy was DSed in constant diameter ampoules the extent of longitudinal macrosegregation decreased with increasing growth speed [57–59].

3.5. Primary dendrite trunk diameter

Under steady-state growth conditions (constant thermal gradient, growth speed and alloy composition) the primary dendrite spacing [60], and the primary dendrite trunk diameter [61], both, are expected

to remain constant along the length of the DSed sample. Therefore, dendrite spacing to trunk diameter ratio is also expected to remain constant along the length. As typically shown in Fig. 10(b), the trunk diameters of primary dendrites were measured on several cross-sections by drawing crosses across the primary arms which join the inter-dendritic eutectic located at the opposite ends. Fig. 10(c) shows the variation in the measured primary dendrite trunk diameter as a function of distance from the neck for the two Pb-5.8 Sb samples grown at 30 and $2.5\,\mu m\,s^{-1}$. The trunk diameter at the neck is larger as compared to that before or after the section-change, $65\,\mu m$ vs. $45\,\mu m$ at $30\,\mu m\,s^{-1}$, and $155\,\mu m$ vs. $120\,\mu m$ at $2.5\,\mu m\,s^{-1}$. The ratio of the experimentally observed median nearest neighbor spacing (λ_{MST}) and the corresponding primary dendrite trunk diameter is plotted in Fig. 10(d). Since the cross-section induced advective flow towards the growing dendrite array decreases the primary spacing, and also increases the trunk diameter, a distinct drop is observed in the (λ_{MST}) to trunk diameter ratio at the neck. The sharp drop at the larger growth speed is especially interesting, because had there been no section-change induced advective flow, the λ_{MST} to trunk diameter ratio would have remained constant along the DSed length; because at this growth speed the 'plume type' thermosolutal convection is virtually absent.

3.6. Influence of cross-change induced advective flow on the ordering of cells/dendrites

Fig. 11 plots the m-σ parameters for the minimum spanning trees obtained for the three samples examined in this study at various cross-sections along their solidified length: Pb-5.8 Sb grown at $30\,\mu m\,s^{-1}$ (thick dashed line with open circular symbols) and $2.5\,\mu m\,s^{-1}$ (thick
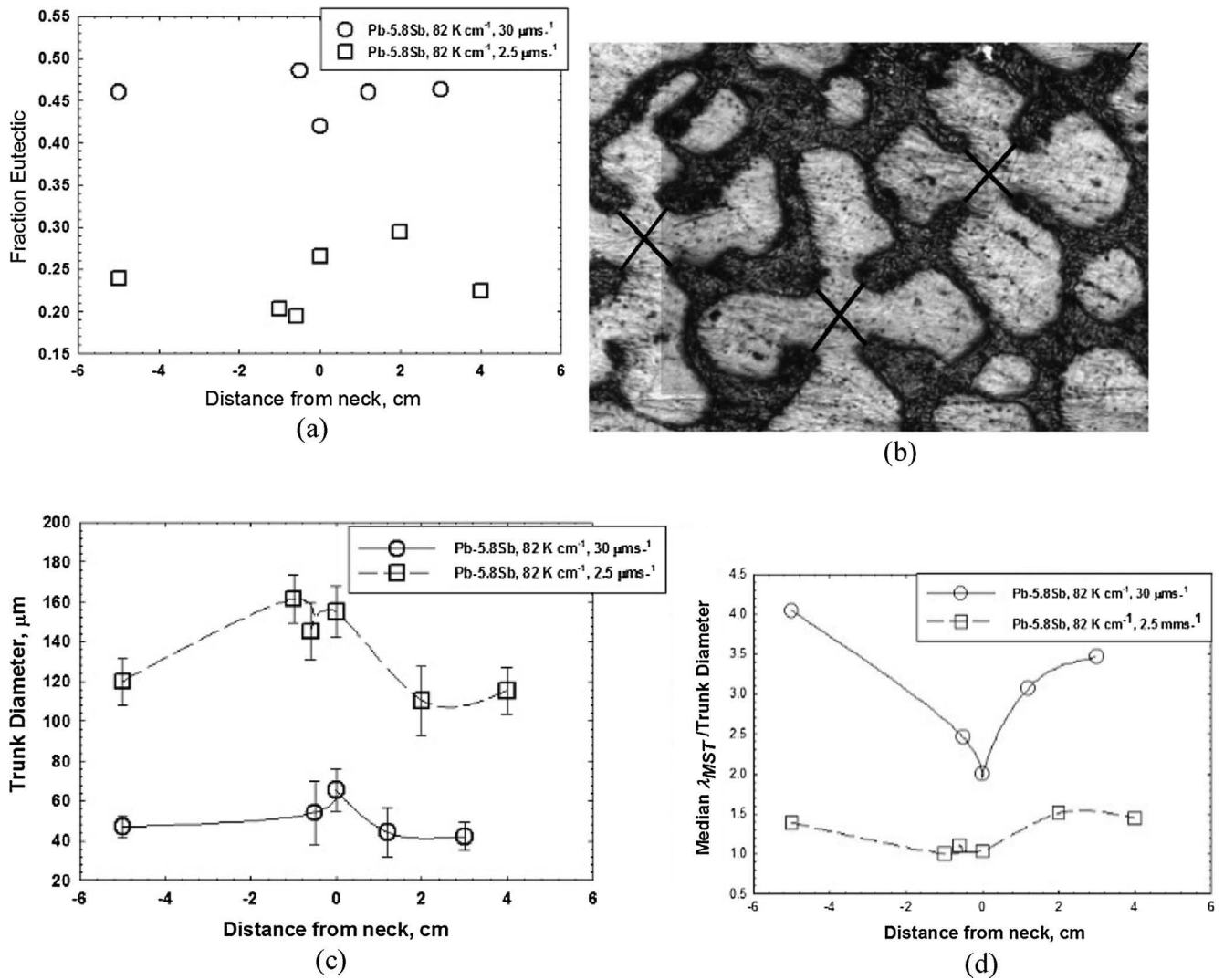
Fig. 10. Influence of cross-section change driven flow on the primary dendrite trunk diameter in Pb-5.8Sb alloy DSed at 30 and 2.5 μm s⁻¹ (82 K cm⁻¹). (a) Longitudinal macrosegregtaion as indicated by area-fraction of eutectic constituent in the transverse microstructure. (b) Typical primary dendrite trunk diameter measurement. (c) Primary dendrite trunk diameter is larger at the neck as compared to before or after the neck. (d) Nearest neighbor spacing to trunk diameter ratio shows a distinct decrease at the constriction, especially at 30 μm s⁻¹.

dotted line with open square symbols), and Pb-2.2 Sb grown at 2.5 μm s⁻¹ (dashed line with open triangular symbols), all with a thermal gradient of 82 K cm⁻¹. The arrow heads along these three lines indicate the path of directional solidification. By following these arrows, one can follow the directional solidification process from the beginning to the end, as the liquid-solid interface moves from the uniform cross-section portion below the neck towards the constriction, and then exits into the uniform cross-section portion above. The "filled" symbols on these three lines correspond to the section at the neck.

The fine dotted line in Fig. 11 represents the *m-σ* behavior for a simulated square-lattice with increasing superimposed random noise. A square lattice would yield m = 1 and σ = 0. The crosses on this line correspond to a 10% noise increment, starting from the perfect square lattice at m = 1 and σ = 0. As disorder is introduced into this lattice by superimposing random noise the *m* value decreases from unity and σ value increases from zero. Clustering of *m-σ* data around this line is an indication of the influence of the underlying long range ordering due to the [1 0 0] seed on the distribution of the primary dendrites. Location of data away from the line indicates loss of such influence.

The triangular symbols in Fig. 11, corresponding to the Pb-2.2Sb alloy sample grown at 2.5 μm s⁻¹ (Fig. 6), indicate that the [1 0 0] single crystal has no influence on the distribution of primary arms with cellular morphology. This is not the case for the well-branched primary dendrites in Pb-5.8 Sb grown at 30 μm s⁻¹ whose *m-σ* values (circular symbols in Fig. 11) are clustered near the line corresponding to the simulated disordered square lattice. The transverse microstructures of this sample (Fig. 2) also showed that the long-range ordering of dendrites initiated by the single-crystal seed was retained throughout the sample length, as the liquid-solid interface traversed through the neck and came back into the uniform cross-section portion of the ampoule.

As shown in Fig. 4(a), the arrangement of the primary dendrites in the uniform cross-section portion below the neck reflected the underlying square-arrangement resulting from the ⟨1 0 0⟩ seed for the Pb-5.8 Sb sample grown at 2.5 μm s⁻¹, a growth condition very close to the cell/dendrite transition. This is also indicated by the first two square symbols of the thick dotted line in Fig. 11, corresponding to the region well below the neck, being located close to the simulated disordered square lattice line. But as the primary dendrites first lose their side-branches, transforming into cells in the constriction region, and then develop their side-branches again while exiting the neck, their initial ordering from the seed is completely lost, as indicated by the location of the final two square symbols on the thick dotted line in Fig. 11. This is due to the formation of new sub-grains made possible by the convection arising from the cross-section change during directional solidification.
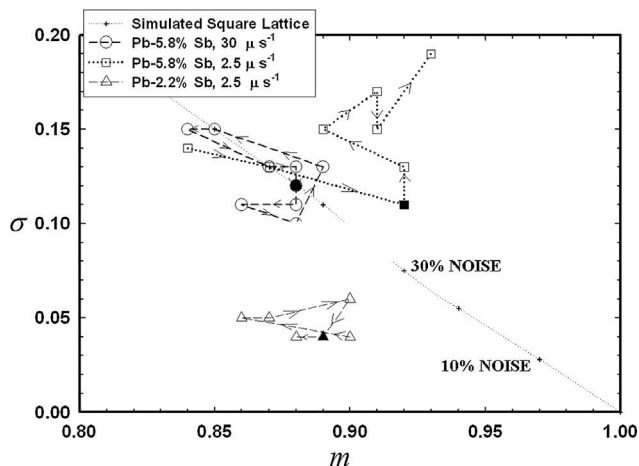
Fig. 11. The m-σ parameters for the minimum spanning trees obtained for the three samples at various cross-sections along their solidified length: Pb-5.8 wt. pct. Sb grown at $30\,\mu m\,s^{-1}$ (thick dashed line with open circular symbols) and $2.5\,\mu m\,s^{-1}$ (thick dotted line with open square symbols), and Pb-2.2 wt. pct. Sb grown at $2.5\,\mu m\,s^{-1}$ (dashed line with open triangular symbols), all with a thermal gradient of $82\,K\,cm^{-1}$. The arrow heads on the lines indicate the direction of the solidification process as the liquid-solid interface moves from the uniform cross-section portion below the neck towards the constriction, and then exits into the uniform cross-section portion above. Exact locations of the neck are marked by filled symbols. The fine dotted line represents the m-σ behavior for a simulated square-lattice with increasing superimposed random noise; the crosses correspond to a 10% noise increment, starting from perfect square lattice at m = 1 and $\sigma = 0$.

Low-speed high thermal gradient growth conditions, close to the cell/dendrite transitions, should, therefore, be avoided during directional solidification of superalloy single-crystal turbine blade components.

4. Discussion

During solidification there is a shrinkage driven (advective) flow towards the liquid-solid interface because of the volume decrease associated with the solidification. As the liquid-solid interface enters the necked portion of the hour-glass shaped ampoule, the solidification of a larger cross-section area at the bottom of the mush has to be fed through a narrower cross-section liquid region at the top which introduces additional advection towards the interface. Therefore, the magnitude of advective flow towards the cellular/dendritic array tips increases as compared with that during solidification in the uniform cross-section region of the sample. The cross-section area at the neck is ¼ of that in the constant diameter portion, and the solidification shrinkage for Pb-6Sb, as reported in Ref. [62] is 3.11%. Therefore, the maximum speed of the flow towards the array tips at the neck could be about 12.4% of the growth speed. The melt ahead of the array tips is not only warmer, it is also solute rich because of the "plume type" thermosolutal convection. The advective flow brings the warmer solute rich melt from ahead of the primary dendrite array towards their tips. This can remelt and suppress the growth of side-branches.

Our ampoule cross-section area decreased over a distance of about 2 cm and then increased over a similar distance. The thermal gradient in the mushy-zone measured from Fig. 1(b) is about $74\,K\,cm^{-1}$, which would make the mushy-zone to be 0.48 cm long for the Pb-5.8Sb alloy, and 0.82 cm long for the Pb-2.2 Sb alloy. The observed morphology changes, as the solidification front enters the neck or exits, therefore, occur over a growth distance which is about 4 times the mushy zone length for Pb-5.8 Sb, and about 2.4 times for Pb-2.2 Sb. It may be noted that our prior experiments have shown that 2 to 3 mushy-zone-length of DS is required for the array to achieve a new steady-state morphology after an abrupt change in the growth speed [63].

Lehmann et al. [64] derived the following relationship between the primary spacing in the absence and in the presence of a convective flow parallel to the primary arms,

$$(\lambda_o/\lambda)^2 - 1 = V_p/R \qquad (3)$$

Here Vp is the fluid velocity, R is the growth speed, and λ_o and λ are primary spacing in the absence and presence of fluid flow. They assumed that the flow velocity parallel to the primary arm remains low enough that the tip undercooling due to curvature remains unaffected. According to Eq. (1), the fluid flowing towards the array tips at 12.4% of the growth speed, estimated above, should result in about 6% decrease in the primary spacing. However, the experimentally observed reductions in the two Pb-5.8Sb alloy samples are much larger, 30% at $30\,\mu m\,s^{-1}$ (Fig. 3(b), λ_A decreased from 180 to 125 μm), and 12.5% at $2.5\,\mu m\,s^{-1}$ (Fig. 5(b) λ_A decreased from 200 to 175 μm).

It may be argued that flow towards the liquid-solid interface provides an efficient mechanism to carry away the solute in the melt being rejected by the process of solidification, thus avoiding the buildup of solute-rich layer and providing stability to the liquid-solid interface against break-down [24–26]. This would explain the cellular to planar liquid-solid interface transition observed at the neck region of the Pb-2.2 Sb alloy sample grown at $2.5\,\mu m\,s^{-1}$ (Fig. 6). The decreased solutal gradient in the melt ahead of the tips would increase the marginal stability wave length [65], and hence result in a larger dendrite-tip radius. An increased tip radius would also increase the primary dendrite trunk diameter [61], as observed in this study (Fig. 10(c)).

However, the large decrease in the primary dendrite spacing and increase in the dendrite shape factor as the liquid-solid interface enters the neck portion cannot be accounted for by the increased tip-radius alone. We believe that as the area-decrease-induced advective flow carrying warmer solute rich melt enters the mushy-zone, it also diminishes the side-branch growth and causes their re-melting. This not only makes the primary dendrites blunter (larger shape factor), it also allows the neighboring primary dendrites to come closer together, resulting in the decreased nearest-neighbor spacing.

Following observations support this view.

(1) The decrease in the primary dendrite spacing as the liquid-solid interface enters the neck portion is always associated with increase in dendrite shape factor (Fig. 3(b) and (c) for the Pb-5.8 Sb alloy grown at $30\,\mu m\,s^{-1}$, and Fig. 5(b) and (c) for the same alloy grown at $2.5\,\mu m\,s^{-1}$). Increase in the dendrite shape factor is a manifestation of reduced side-branch growth near the array tips. In addition, the reverse effect is seen as the liquid-solid interface emerges from the necked portion into the uniform cross-section portion of the ampoule (Fig. 3(b) and (c) for the Pb-5.8 Sb alloy grown at $30\,\mu m\,s^{-1}$, and Fig. 5(b) and (c) for the same alloy grown at $2.5\,\mu m\,s^{-1}$).
(2) Larger reduction in the primary dendrite spacing due to cross-section area change is observed for those growth conditions that produce more well-branched primary dendrites; those growing at higher degree of constitutional super-cooling and having longer side-branches. For example, there is a decrease of about 47-μm in the median nearest neighbor spacing for the Pb-5.8 Sb alloy grown at $30\,\mu m\,s^{-1}$ (Fig. 3(b)) versus only about 12-μm for the same alloy grown at the lower growth speed of $2.5\,\mu m\,s^{-1}$ (Fig. 5(b)).
(3) Larger reduction in the primary dendrite spacing due to cross-section area change is observed for alloy compositions that produce more permeable mushy zone. For example, for the identical growth speed of $30\,\mu m\,s^{-1}$ the Pb-10.8 Sb alloy shows a decrease of about 70-μm in the median nearest neighbor spacing, from about 145 to 75-μm (Fig. 9), as compared with 47-μm, from 177 to 130-μm, for the Pb-5.8 Sb alloy (Fig. 3(b)).

It is interesting to note that cellular arrays having no side-branches

also show a slight decrease in their spacing as the liquid-solid interface enters the necked portion of the ampoule. For example, the median nearest neighbor spacing decreases from about 222 to 208-μm for the Pb-2.2 Sb alloy growing at 2.5 μm s^{-1} (Fig. 7(b)). Since the cells do not have side-branches and their mushy-zone permeability is negligible the decrease in their spacing must be entirely associated with the changes in their tip morphology caused by the flow.

It would be interesting to carryout directional solidification and abrupt quench studies in Pb-Sb alloys in similar hourglass shaped ampoules and measure the cell tip radius and the concentration gradients in the melt immediately ahead of the array tips to elucidate the role of parallel flow on the cell/dendrite tip morphology.

Acknowledgements

References

[1] M.C. Flemings, G.E. Nereo, Macrosegregation: Part I: Trans TMSAIME 239 (1967) 1449–1461.
[2] M.C. Flemings, R. Mehrabian, G.E. Nereo, Macrosegregation: Part II: Trans TMS-AIME 242 (1968) 41–49.
[3] M.C. Flemings, G.E. Nereo, Macrosegregation: Part III: Trans TMS-AIME 242 (1968) 50–55.
[4] T.S. Piwonka, P.N. Atanmo, Multicomponent Macrosegregation in a Vacuum Melted Directionally Solidified Superalloy, Vacuum Metallurgy. Science Press, Princeton, N.J., 1977, pp. 507–541.
[5] R. Sellamuthu, M.S. Thesis, University of Pittsburgh, Pittsburgh, PA, 1979.
[6] W.C.S. Wang, M.S. Thesis, The University of Arizona, Tucson, AZ, 1983.
[7] R. Sellamuthu, H.D. Brody, A.F. Giamei, Met. Trans. B 17 (2) (1986) 347–356.
[8] S. Felicelli, D. Poirier, J. Heinrich, J. Cryst. Growth 177 (1–2) (1997) 145–161.
[9] S.D. Felicelli, D.R. Poirier, A.F. Giamei, J.C. Heinrich, JOM 49 (3) (1997) 21–25.
[10] S.D. Felicelli, J.C. Heinrich, D.R. Poirier, Int. J. Num. Method. Fluids 27 (1–4) (1998) 207–227.
[11] S.D. Felicelli, D.R. Poirier, P.K. Sung, Metall. Trans. B 31 (6) (2000) 1283–1292.
[12] D. Ma, J. Ziehm, W. Wang, A. Buhrig-Polaczek, The 3rd international conference on advances in solidification processes, IOP Conf. Ser.: Mater. Sci. Eng. 27 (2011) 012034.
[13] M. Ghods, M. Lauer, R.N. Grugel, S.N. Tewari, D.R. Poirier, J. Mater. Eng. Perform. 26 (10) (2017) 4876–4889.
[14] M. Ghods, M. Lauer, R.N. Grugel, S.N. Tewari, D.R. Poirier, J. Cryst. Growth 459 (2017) 135–145.
[15] M. Ghods, L. Johnson, M. Lauer, S.N. Tewari, R.N. Grugel, D.R. Poirier, J. Cryst. Growth 449 (2016) 134–147.
[16] M. Rappaz, C.A. Gandin, J.L. Desbiolles, P. Thevoz, Metall. Mater. Trans. A 27 (3) (1986) 695–705.
[17] C.A. Gandin, M. Rappaz, Acta Metall. Mater. 42 (7) (1994) 2233–2246.
[18] C.A. Gandin, J.L. Desbiolles, M. Rappaz, P. Thevoz, Metall. Mater. Trans. A 30 (12) (1999) 3153–3165.
[19] A. Kermanpur, M. Rappaz, N. Varahram, P. Davami, Metall. Mater. Trans. B 31 (6) (2000) 1293–1304.
[20] H. Hao, W. Jiang, G. Xie, G. Zhang, Y. Lu, J. Zhang, L. Lou, Prog. Nat. Sci. Mater. Int. 23 (2) (2013) 211–215.
[21] F.U. Wang, Z. Wu, C. Huang, D. Ma, J. Jakumeit, A. Buhrig-Polazek, Metall. Mater. Trans. 48A (2017) 5924–5939.
[22] W. Xuan, C. Li, D. Zhao, B. Wang, C. Li, Z. Ren, Y. Zhong, X. Li, C. Cao, Metall.

[23] D. Ma, Q. Wu, A. Buhrig-Polaczek, Metall. Mater. Trans. 43B (2012) 344–353.
[24] S.H. Davis, Handbook of crystal growth I fundamentals, Part B: transport and stability, in: D.T.J. Hurle (Ed.) North Holland, Amsterdam, 1993, pp. 859–897.
[25] R.T. Delves, Crystal growth, in: B.R. Pamplin (Ed.) Pergamon, Oxford, U.K., 1975, pp. 40–103.
[26] S.R. Coriell, B.T. Murray, A.A. Chernov, G.B. McFaddden, Metall. Mater. Trans. A 27A (1996) 687–694.
[27] T. Huang, S. Liu, Y. Yang, D. Lu, Y. Zhou, J. Cryst. Growth 128 (1993) 167–172.
[28] T. Huang, L. Deyang, Z. Yaoche, Acta Astronautica 12 (9) (1988) 997–1002.
[29] H. Esaka, T. Taenaka, H. Ohishi, S. Mizoguchi, H. Kajioka, International Symposium on Scale Modeling, July 18–22, 1988, Tokyo, The Japan Society of Mechanical Engineers, 1988, pp. 287–293.
[30] T. Okamoto, K. Kishitake, I. Bessho, J. Cryst. Growth 29 (1975) 131–136.
[31] N. Shevchhenko, O. Roshchupkina, O. Sokolova, S. Eckert, J. Cryst. Growth 417 (2015) 1–8.
[32] N. Shevchhenko, S. Boden, G. Gerbeth, S. Eckert, Metall. Mater. Trans. 44A (2013) 3797–3808.
[33] R. Trivedi, H. Miyahara, P. Mazumder, E. Simsek, S.N. Tewari, J. Cryst. Growth 222 (2000) 365–379.
[34] Q. Min, L. Lin, T. Feng_tao, Z. Jun, F. Heng-Zhi, Trans. Nonferrous Met. Soc. China 19 (2009) 1–8.
[35] M.D. Dupouy, D. Camel, J.J. Favier, Acta. Metall. Mater. 37 (4) (1989) 1143–1157.
[36] J.E. Spinelli, O.F.L. Rocha, A. Garcia, Mater. Rsch. 9 (2006) 51–57.
[37] M.D. Dupouy, D. Camel, J.J. Favier, Acta Metall. 40 (7) (1992) 1791–1801.
[38] J.R. Cahoon, M.C. Chaturvedi, K.N. Tandon, Metall. Mater. Trans. A 29A (1998) 1101–1109.
[39] M.D. Dupov, D. Camel, J. Cryst. Growth 183 (1998) 469–489.
[40] H.N. Thi, Y. Dabo, B. Drevet, M.D. Dupouy, D. Camel, B. Billia, J.D. Hunt, A. Chilton, J. Cryst. Growth 281 (2005) 654–668.
[41] B. Drevet, H.N. Thi, D. Camel, B. Billia, M.D. Dupouy, J. Cryst. Growth 218 (2000) 419–433.
[42] G. Zimmerman, A. Weiss, Microg. Sci. Tech. XVI (2005) 143–147.
[43] F.L. Mota, N. Bergeon, D. Touret, A. Karma, R. Trivedi, B. Billia, Acta Mater. 83 (2015) 362–377.
[44] M. Xu, L.M. Fabietti, Y. Song, D. Touret, A. Karma, R. Trivedi, Scripta Mater. 88 (2014) 29–32.
[45] S.N. Tewari, R. Shah, H. Song, Metall. Mater. Trans. A 25A (1994) 1535–1544.
[46] Z. Min, J. Shen, Z. Feng, L. Wang, L. Wang, H. Fu, J. Cryst. Growth 320 (2011) 41–45.
[47] X. Li, A. Gagnoud, Y. Fautrelle, R. Moreau, D. Du, Z. Ren, Z. Lu, Metall. Mater. Trans. A 47A (2016) 1198–1214.
[48] S. Steinbach, L. Ratke, Metall. Mater. Trans. A 38A (2007) 1388–1394.
[49] I. Steinback, Acta Mater. 57 (2009) 2640–2645.
[50] L. Yuan, P.D. Lee, Modell. Simul. Mater. Sci. Eng. 18 (2010) 055008.
[51] S. Karagadde, L. Yuan, N. Shevchenko, S. Eckert, P.D. Lee, Acta Mater. 79 (2014) 168–180.
[52] Z. Gao, J. Mi, S. Xiong, P.S. Grant, Metall. Mater. Trans. B 44B (2013) 924–937.
[53] L.M. Fabietti, V. Seetharaman, R. Trivedi, Metall. Trans. A 21A (1990) 1299–1310.
[54] V.E. Zinov'ev, Handbook of Thermophysical Properties of Metals at High Temperatures, Nova Science Publ, New York, N.Y., 1996, p. 159.
[55] C. Dussert, G. Rasigni, M. Rasigni, J. Palmari, A. Liebaria, Phys. Rev. 34B (1986) 3528–3529.
[56] C. Ghods, L. Johnson, M. Lauer, S.N. Tewari, R.N. Grugel, D.R. Poirier, J. Cryst. Growth 449 (2016) 107–116.
[57] S.N. Ojha, G. Ding, Y. Lu, J. Rye, S.N. Tewari, Metall. Mater. Trans. A 30A (1999) 2167–2171.
[58] S.N. Ojha, S.N. Tewari, Int. J. Cast Metals Res. 13 (2000) 207–213.
[59] S.N. Tewari, R. Tiwari, Metall. Mater. Trans. A 34A (2003) 2365–2376.
[60] S. Lu, J.D. Hunt, J. Cryst. Growth 123 (1992) 17–34.
[61] S.N. Tewari, R.N. Grugel, D.R. Poirier, Metall. Mater. Trans. 45A (2014) 4758–4761.
[62] Metals Handbook, vol. 2, ninth edition, American Society for Metals, Metals Park, OH 44073, 1979, p. 507.
[63] H. Chen, Y.S. Chen, X. Wu, S.N. Tewari, J. Cryst. Growth 253 (2003) 413–423.
[64] P. Lehmann, R. Moreaue, D. Camel, R. Bocato, J. Cryst. Growth 183 (1998) 690–704.
[65] W.W. Mullins, R.F. Sekerka, J. Appl. Phys. 35 (1964) 444–451.